Environmental Science & Technology

Article

pubs.acs.org/est

In Situ Spatially and Temporally Resolved Measurements of Salt Concentration between Charging Porous Electrodes for Desalination by Capacitive Deionization

Matthew E. Suss,[†,‡] P.M. Biesheuvel,[§,⊥] Theodore F. Baumann,[‡] Michael Stadermann,[‡] and Juan G. Santiago*[,†]

[†]Department of Mechanical Engineering, Stanford University, 440 Escondido Mall, Stanford, California 94305, United States

[‡]Lawrence Livermore National Laboratory, 7000 East Avenue, Livermore, California 94551, United States

[§]Wetsus, Centre of Excellence for Sustainable Water Technology, Agora 1, 8934 CJ, Leeuwarden, The Netherlands

[⊥]Department of Environmental Technology, Wageningen University, Borne Weilanden 9, 6708 WG, Wageningen, The Netherlands

Supporting Information

ABSTRACT: Capacitive deionization (CDI) is an emerging water desalination technique. In CDI, pairs of porous electrode capacitors are electrically charged to remove salt from brackish water present between the electrodes. We here present a novel experimental technique allowing measurement of spatially and temporally resolved salt concentration between the CDI electrodes. Our technique measures the local fluorescence intensity of a neutrally charged fluorescent probe which is collisionally quenched by chloride ions. To our knowledge, our system is the first to measure in situ and spatially resolved chloride concentration in a laboratory CDI cell. We here demonstrate good agreement between our dynamic measurements of salt concentration in a charging, millimeter-scale CDI system to the results of a modified Donnan porous electrode transport model. Further, we utilize our dynamic measurements to demonstrate that salt removal between our charging CDI electrodes occurs on a longer time scale than the capacitive charging time scales of our CDI cell. Compared to typical measurements of CDI system performance (namely, measurements of outflow ionic conductivity), our technique can enable more advanced and better-controlled studies of ion transport in CDI systems, which can potentially catalyze future performance improvements.

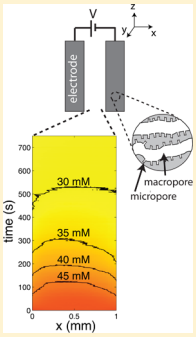

INTRODUCTION

Capacitive deionization (CDI) is an emerging water desalination technique which uses a porous electrode capacitor to remove salt ions from brackish water.[1] A typical CDI cell consists of two porous carbon electrodes separated by a porous separator element or an open channel. A voltage of roughly 1 V is applied across the porous electrodes, causing salt ions to electromigrate to the oppositely charged electrode and to be held electrostatically in electric double layers (EDLs) at the pore surface.[2−4] The most common architecture of a CDI cell is a flow-between architecture, whereby the feedwater flows between the two charging porous electrodes.[1,5−7] Alternative CDI architectures can use flow-through electrodes to enable faster and more efficient desalination,[8] ion exchange membranes along electrode surfaces to improve electrode charge efficiency,[9−11] or flow electrodes to enable desalination of high salinity feedwaters such as seawater.[12] Once charged, the CDI cell must then be discharged to allow for subsequent desalination cycles.[1] Discharging releases salt held in the EDLs, resulting in a brine solution.[13]

Since investigations into CDI-type systems began in the 1960s,[14] the most widely used experimental technique to investigate CDI system desalination performance has been conductivity measurements of the system's effluent.[1,8,15−25] This typically involves a conductivity sensor placed in series with, and downstream of, the CDI system. The latter technique is well suited for characterizing and evaluating the desalination performance of CDI cells; however, it is not as well suited for spatially resolved studies of ion transport in CDI systems. Notably, conductivity measurements can be affected by flow effects in the cell and the rest of the system components, such as mechanical or hydrodynamic dispersion, and typically cannot provide information on the contributions of individual electrodes. Classical electrochemical techniques such as cyclic voltammetry (CV) and electrochemical impedance spectroscopy (EIS) are often used to characterize CDI cell or individual CDI electrode capacitance,[24,26,27] but the data from these techniques can be difficult to interpret for CDI cells performing desalination, as the desalination process is not reasonably represented by linear circuit models.[28] Thus, a technique which can perform in situ (in a laboratory cell) measurements with spatial and temporal resolution of salt concentration in a charging CDI cell represents a significant advance in the experimental study and diagnostics of CDI cell performance. Such a technique can be used to study ion transport and

Received: August 21, 2013
Revised: January 7, 2014
Accepted: January 8, 2014
Published: January 8, 2014

   dx.doi.org/10.1021/es403682n | Environ. Sci. Technol. 2014, 48, 2008−2015

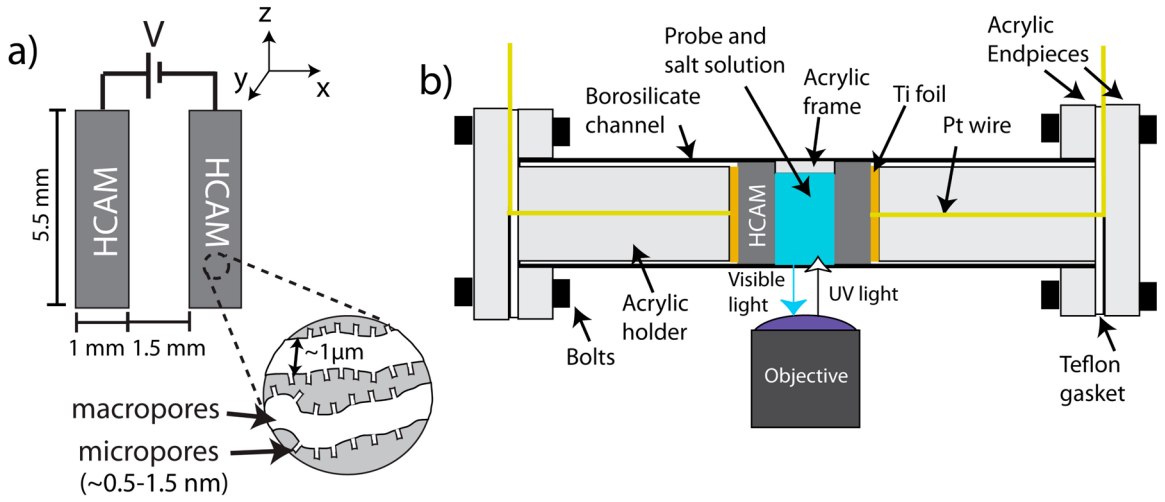

Figure 1. (a) Schematic of the capacitive deionization (CDI) cell used in this study. The cell consists of two 1 mm thick hierarchical carbon aerogel monolith (HCAM) electrodes which were held 1.5 mm apart. The HCAM electrodes have a hierarchical pore structure consisting of micrometer-scale "macropores" and nanoscale "micropores". (b) Schematic of a cross section of the setup used to visualize ion dynamics between two porous HCAM electrodes. The 1 mm thick electrodes were inserted into a transparent borosilicate glass channel and separated by a distance of 1.5 mm using a thin acrylic frame/spacer. The acrylic frame is three sided, with an open fourth side which permits UV light to enter into a 5 × 5 × 1.5 mm space between electrodes. The electrodes and space between them is filled with a KCl salt and SPQ probe solution. UV light excites the chloride-sensing SPQ, whose fluorescent emissions are captured by our microscope objective and CCD camera.

desalination in the presence or absence of flow and can enable well-controlled, fundamental studies, the results of which can potentially guide performance enhancements.

In this work, we demonstrate a simple and novel experimental system for in situ measurements of spatially and temporally resolved salt concentration *between* electrodes in an actively charging CDI cell. Our system measures the local fluorescence signal of a neutral (thus uncharged) probe molecule added to the background salt-water solution. This probe molecule's fluorescence is quenched by collisions with chloride ions.[29] As the probe is neutral, it does not electromigrate within our charging CDI cell, and we thus can simply correlate local fluorescence intensity between our charging electrodes to local chloride ion (salt) concentration. Our system is, to our knowledge, the first to demonstrate in situ temporally and spatially resolved measurements of chloride concentration in a CDI cell. Demirer et al. presented visualizations of charged dye species in a microfluidic CDI system with microfabricated pseudoporous electrodes.[30] Their cell contained an aqueous solution with the charged (ionic) dye species at about 1 μM concentrations, and they correlated fluorescence intensity to local dye concentration.[30] The latter technique was not used to measure the concentration of a nonfluorescent salt in a CDI cell (e.g., NaCl) and may not be well suited for such measurements (as charged dyes can themselves electromigrate). Roelofs et al. also performed visualizations of charged dyes in a microfluidic CDI-type system, and utilized a dye with pH dependent fluorescence to observe the onset of pH waves from planar electrodes.[31] Sharma et al. utilized neutron imaging applied to a CDI cell to visualize the local concentration of gadolinium ions both within the pore space of mesoporous carbon electrodes and between the electrodes.[32] In this work, we measure the local chloride concentration between the electrodes of a charging, realistically sized (millimeter to centimeter scale) CDI cell using a benchtop fluorescence microscope. We further compare our measurements to a modified Donnan (mD) CDI dynamic transport model.[33] Importantly, we here study the desalination dynamics in a cell without flow, whereas in future studies flow can be included, and its effects on the charging dynamics are studied separately.

THEORY

In this section, we describe the dynamic transport model based on porous electrode theory, which we used to compare to our experimental data. We used a modified Donnan (mD) model for the electric double layer (EDL) structure, which has been used to model desalination in CDI systems using multiscale porous electrodes.[33,34] The transport model assumes an electrode pore structure which is composed of larger transport pathways (interparticle pore space) located between micrometer-scale carbon particles (form this point onward, we term these pores "macropores"; to indicate features which have typically >50 nm characteristic scales) and the smaller intraparticle pores (which we will term "micropores"; and which typically have <2 nm characteristic scales). Fluid flow, ion diffusion, and ion electromigration in the electroneutral macropores occur in response to, respectively, hydrostatic pressure, species concentrations, and potential gradients in those pores. We establish a "cell voltage" by applying a voltage step between the two porous electrodes. The subsequent charging of the porous electrodes causes salt ions to be transported from the solution into EDLs. Since the micropores account for most of the surface area, there is a net salt transport from macropores into micropores. As the Debye length characterizing EDL thickness is approximately 1−10 nm for typical CDI cell feedwater salt concentrations, the mD model assumes that the EDLs lining the micropore walls are strongly overlapped. Thus, the electric potential in these pores is assumed to be uniform. Here, a Donnan potential drop, $\Delta\varphi_D$, exists between the equipotential micropore and its adjacent macropore. The term "modified" is used, as this model accounts for a Stern layer in the micropore EDL, and in addition accounts for an additional contribution to transport of salt into the micropores (from physi- or chemisorption interactions between the carbon surface and the salt ions).[33]

dx.doi.org/10.1021/es403682n | *Environ. Sci. Technol.* 2014, 48, 2008−2015

To develop this model, we consider a one-dimensional geometry along the x direction (along a straight line between the two electrodes, as shown in Figure 1a). We assume a quiescent fluid in the cell, uniform porosity throughout the electrode, and a binary, symmetric, univalent, and dilute electrolyte. We here assume equal ion diffusion coefficients, D; as in our experiments, we will use symmetric KCl solutions ($D \cong 1.8 \times 10^{-9}$ m^2/s when including the effects of finite solution ionic strength[35]). Thus, the conservation of salt in a porous, multiscale electrode consisting of macro- and micropores is expressed as:

$$p_{mA}\frac{\partial c_{mA}}{\partial t} + \frac{p_{mi}}{2}\frac{\partial c_{mi}}{\partial t} = \frac{\partial}{\partial x}\left(p_{mA}D\frac{\partial c_{mA}}{\partial x}\right) \quad (1)$$

Here, c_{mA} is the salt concentration in the electroneutral macropores, and c_{mi} is the total concentration of ions in the micropores ($c_{mi} = c_{mi,a} + c_{mi,c}$, where the subscripts a and c refer to anions and cations, respectively). These concentrations are quantities volume averaged over scales larger than the macropore topologic features but small compared to the electrode and cell dimensions. In the macropores (and between electrodes), the local concentration of anions equals that of the cations via the electroneutrality condition,[36,37] and thus, $c_{mA,a} = c_{mA,c} = c_{mA}$ (and we can use the terms "ion concentration" and "salt concentration" interchangeably). In the micropore, anion and cation concentrations are not equal in order to balance the solid wall surface charge. Further, p_{mA} and p_{mi} are the porosities associated with macro- and micropores, respectively, defined per volume of the total electrode assembly (not, e.g., defined per carbon particle volume). We can further write a balance of charge equation as:

$$p_{mi}\frac{\partial \sigma_{mi}}{\partial t} = \frac{\partial}{\partial x}\left(2p_{mA}Dc_{mA}\frac{\partial \varphi}{\partial x}\right) \quad (2)$$

$$\sigma_{mi} \equiv c_{mi,c} - c_{mi,a} \quad (3)$$

For univalent species, $\sigma_{mi}F$ is the excess positive volumetric charge density in the micropores, where F is the Faraday constant and φ is the local nondimensional potential in the macropore (dimensional potential is normalized by V_T, where V_T is the thermal voltage, given by $V_T = RT/F = k_BT/e$ where T is temperature, R is the ideal gas constant, k_B is the Boltzmann constant, and e is the elementary charge). The total potential drop between the solid (carbon) phase, φ_1, and the local macropore liquid phase is:

$$\varphi_1 - \varphi = \Delta\varphi_D + \Delta\varphi_{st} \quad (4)$$

where $\Delta\varphi_D$ is the Donnan potential and $\Delta\varphi_{st}$ is the potential drop across the Stern layer. Assuming equilibrium between the micro- and macropore, we can write the following relation for concentration of ion i in the micropore:

$$c_{mi,i} = c_{mA}\exp(-z_i\Delta\varphi_D + \mu_{att,i}) \quad (5)$$

Here, z_i is the valence of ion i, and $\mu_{att,i}$ is a nondimensional potential that acts as an additional driving force for ions to enter into micropores. Last, we invoke the definition of capacitance to link σ_{mi} to the potential drop across the micropore Stern layer:

$$\sigma_{mi} = -\frac{C_{st,vol}\Delta\varphi_{st}V_T}{F}. \quad (6)$$

Here, $C_{st,vol}$ is the volumetric micropore Stern layer capacitance. Previous studies on activated carbon electrodes have shown that often $C_{st,vol}$ must be allowed to increase slightly with $\Delta\varphi_{st}$ or σ_{mi} in order to describe data accurately.[1] We can describe c_{mi} and σ_{mi} in terms of the Donnan potential and c_{mA} (and assuming that $\mu_{att,a} = \mu_{att,c} = \mu_{att}$[33]), which gives us our final set of equations:

$$p_{mA}\frac{\partial c_{mA}}{\partial t} + p_{mi}\frac{\partial\left(\sigma_{mi}^2/4 + \left[c_{mA}e^{\mu_{att}}\right]^2\right)^{1/2}}{\partial t} = \frac{\partial}{\partial x}\left(p_{mA}D\frac{\partial c_{mA}}{\partial x}\right) \quad (7)$$

$$p_{mi}\frac{\partial \sigma_{mi}}{\partial t} = \frac{\partial}{\partial x}\left(2p_{mA}Dc_{mA}\frac{\partial \varphi}{\partial x}\right) \quad (8)$$

$$\varphi = \varphi_1 + \sinh^{-1}(\sigma_{mi}/2c_{mA}e^{\mu_{att}}) + \sigma_{mi}F/(C_{st,vol}V_T) \quad (9)$$

We also included in our model domain a separator layer between the porous electrodes, as is in our experimental cell (see Figure 1a). In the section of the model domain representing the separator ($l_e \le x \le l_e+l_s$, where l_e is the electrode thickness and l_s is the separator thickness), we removed the salt and charge sink terms in eqs 7 and 8 (terms led by the factor p_{mi}). Thus, σ_{mi} is not a dependent variable in the space between electrodes, and we did not solve for eq 9 in this part of the domain. Further, in the separator, the parameter p_{mA} in the model was replaced by the porosity of the separator layer, p_s. For an open (nonporous) separator, p_s can be set to unity. At the internal boundaries of our model domain representing the electrode−separator interface ($x = l_e$ and $l_s + l_e$), we ensured the continuity of c_{mA} and φ, as well as imposed a matching condition for salt flux and of ionic current:

$$p_{mA}\left.\frac{\partial c_{mA}}{\partial x}\right|_e = p_s\left.\frac{\partial c_{mA}}{\partial x}\right|_s \quad (10)$$

$$p_{mA}\left.\frac{\partial \varphi}{\partial x}\right|_e = p_s\left.\frac{\partial \varphi}{\partial x}\right|_s \quad (11)$$

The latter flux conditions can cause a discontinuity in concentration and potential gradients across these internal boundaries due to a discontinuity in porosity. To mimic the conditions of our experimental cell (see Figure 1b), we used zero ionic current ($\partial\varphi/\partial x = 0$) and salt flux ($\partial c_{mA}/\partial x = 0$) boundary conditions at the outer surfaces of the electrodes ($x = 0$ and $x = l_s + 2l_e$). For initial conditions, we assumed a uniform concentration in the cell, c_o (i.e., in the separator layer and in the macropores of the electrodes), and zero net charge in the micropores ($\sigma_{mi} = 0$ for all x). Because of the nonzero value of μ_{att}, there is a net salt adsorption in the micropores, and so $c_{mi}/2 > c_{mA}$ initially. For the model calculations, we assumed a symmetric CDI cell, and thus, the applied cell voltage relates to the solid phase electrode potential (relative to the midplane), φ_1, by: $V_{cell} = 2\varphi_1V_T$.

EXPERIMENTAL METHODS

CDI Cell Design. In Figure 1a, we show a schematic of the CDI cell used in this study. Our CDI cell consisted of two, custom-fabricated hierarchical carbon aerogel monolith (HCAM) electrodes. Each electrode had a cross section (normal to the electric field direction) of approximately 5.7 × 5.7 mm and was 1 mm thick along the x direction. The HCAM electrode pore structure consists of a micrometer-scale pore network (so-called "macropores"), with nanoscale pores

subsequently etched into the carbon surfaces through the process of thermal activation (so-called "micropores").[38,39] In this work, we use HCAM electrodes which had been thermally activated (exposed to CO_2 at 950 °C) for 2 h. The rest of the steps in fabrication of the HCAMs used in this study are as described in Baumann et al.[38] HCAM electrodes have previously been utilized in flow-through electrode capacitive desalination systems[8] and as electric double layer capacitor energy storage systems.[39] We measured the total porosity ($p_{mA} + p_{mi}$) of our HCAM electrode as approximately 0.77 using dry/water-saturated measurements of the electrode mass. From previously reported N_2 adsorption porosimetry measurements,[27] we estimate that our electrode has a porosity associated with the micropores, p_{mi}, of about 0.2, and so, we can approximate $p_{mA} = 0.77 - p_{mi} = 0.57$. In our CDI cell, the HCAM electrodes were separated by a distance of 1.5 mm. The step voltage applied to the cell, V_{cell}, varied between 0.25 and 1.25 V.

Experimental Setup. In Figure 1b, we show a schematic of the experimental setup used for visualizations of salt concentration between two charging electrodes. In this system, we inserted the two HCAM electrodes into a transparent, 1.6 cm long, square borosilicate channel with a 5.9 × 5.9 mm internal cross section (Friedrich & Dimmock Inc., Millville, NJ, USA). Between the electrodes, we place a 5.8 × 5.8 mm acrylic frame with a thickness (along the x direction) of 1.5 mm (McMaster-Carr, Santa Fe Springs, CA, USA). The frame was three sided, with a slot of 5 × 5 × 1.5 mm laser cut into the open fourth side (Universal Laser Systems, Scottsdale, AZ, USA). The slot's purpose was to allow for optical access into the space between the two HCAM electrodes. Two 5 × 5 mm, 127 μm thick titanium foil sheets (Alfa Aesar, Ward Hill, MA, USA) were inserted into the borosilicate channel and contacted with the outward-facing ends of the HCAM electrodes. Acrylic rectangles (so-called "holders" in Figure 1b) with cross-section dimensions of 5.8 × 5.8 mm and length (along the x direction) of 6.1 mm were placed behind the titanium foil, and a platinum wire was inserted through a hole drilled into the center of the "holder" to contact the foil. The platinum wire was used contact the external power supply (Keithley 2410, Cleveland, OH, USA) to the titanium foil current collector. On each side of the glass channel, two 1.5 mm thick acrylic end plates were bolted together, sandwiching a compressible expanded Teflon gasket, in order to seal the setup and compress the setup components for good electrical contact. Both end plates had external dimensions of 2 × 2 cm, and one end plate had a 7.6 × 7.6 mm window laser cut into its center in order to slip it over the borosilicate channel's outer walls. For all visualizations, we used an inverted epifluorescent microscope (Eclipse TE300, Nikon, Japan), a 4×, NA 0.2 objective (Nikon, Japan), and captured images with a CCD camera (PI-MAX: 512, Princeton Instruments, Trenton, NJ, USA) with a 24 μm pixel width. Further, we used a 11000v3 Chroma filter cube (Chroma, Bellows Falls, VT, USA) with peak excitation wavelength range of roughly 320−380 nm and broadband emission beyond 420 nm.

Chloride Ion Concentration Measurements. We measured spatially and temporally resolved salt concentration in the space between charging HCAM electrodes using species-altered fluorescence imaging (SAFI).[29] As our fluorescent probe, we use 6-methoxy-*N*-(3-sulfopropyl)quinolinium (SPQ) (Santa Cruz Biotechnology Inc., Dallas, TX, USA). SPQ is excited by UV light at about 344 nm and subsequently emits visible light with peak intensity at 443 nm. SPQ fluorescence emissions are collisionally quenched by chloride ions (as well as other halide ions such as bromide and iodide [29]), and its fluorescence intensity in a chloride ion containing salt solution (in the absence of other quenchers) can be described by a Stern−Volmer equation:[40]

$$\frac{I_o}{I} = 1 + K_{Q,cl^-}[c_{cl^-}] \tag{12}$$

where I_o is the fluorescence intensity at zero chloride ion concentration, I is the intensity at a chloride ion concentration of c_{cl^-}, and K_{Q,cl^-} is the quenching constant, which is 107 M^{-1} for a salt solution with solely chloride as the anions.[41] A key feature of SPQ is that it is neutrally charged and so does not electromigrate despite the presence of an electric field in our charging CDI cell.[29] Thus, changes in observed SPQ fluorescence can be attributed to changing chloride ion concentration. We related measured SPQ fluorescence to local chloride ion concentration with the following equation, derived from eq 12:

$$[c_{cl^-}] = \frac{1}{K_{Q,cl^-}}\left(\frac{I_{ref}}{I}(1 + K_{Q,cl^-}[c_{cl^-,ref}]) - 1\right) \tag{13}$$

I_{ref} is the fluorescence intensity measured at a reference concentration, $c_{cl^-,ref}$. In our experiments, the reference fluorescence is that of the initial (undesalted) solution before application of the cell voltage.

Experimental Protocol. In all experiments, we used an electrolyte consisting of a mixture of KCl salt and SPQ probe. We used KCl because the ionic mobilities of the K^+ and Cl^- ions are approximately equal, and thus, our experiments more closely adhered to the assumptions used in the porous electrode transport model (see Theory section). We used KCl solutions with concentrations of either 50 or 80 mM and an SPQ concentration of 5 mM in all experiments.

The following protocol was used in all experimental results presented in this work. For at least 12 h before experiments, each HCAM electrode was soaked in a 10 mL solution of either 50 or 80 mM KCl and 5 mM SPQ (where each electrode held <100 μL of solution in its pore space). The latter soak allowed ample time for specific (nonelectrostatic) adsorption of the salt and probe solutes to the carbon surfaces, in an effort to ensure that equilibrium between the porous carbon and solution was reached. Visualization experiments conducted without application of an electric field demonstrated that no significant specific adsorption occurred after this soak (measured fluorescence intensity remained largely unchanged over experimental time scales). On any single day, experiments were performed with a single KCl concentration. Changing the KCl concentration used in our experiments was preceded by a 12 h soak with the new concentration. This latter procedure allowed the HCAM electrodes to come to equilibrium with the pertinent KCl and SPQ solution prior to running the respective experiment. Immediately before an experiment, we inserted all the components into the borosilicate channel, filled the space between the electrodes with the same KCl and SPQ solution as in the electrode pore space, and sealed the endpieces (see Figure 1b). We then imaged SPQ fluorescence in the space between the HCAM electrodes using our optical setup for a period of at least 20 s (at 1 frame per second) before applying the cell voltage and imaging the spatially resolved, dynamic SPQ fluorescence signal for at least another 1000 s (1000

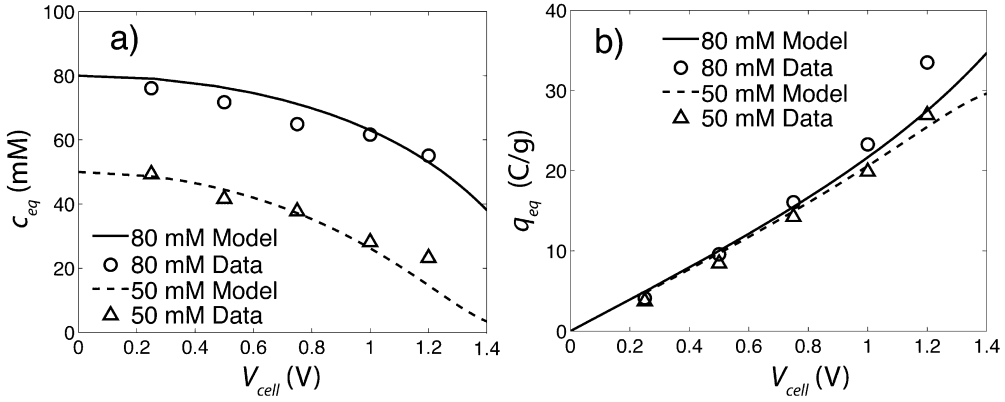

Figure 2. Model result and measured (a) equilibrium salt concentration, c_{eq}, and (b) equilibrium charge stored, q_{eq}, vs applied potential for initial salt concentrations of 50 and 80 mM. Measured data for c_{eq} is obtained from visualizations and q_{eq} from current measured for the two-electrode cell. The model lines are obtained from the modified Donnan (mD) model results.

frames). The raw visualization signal was background subtracted and normalized by a flatfield. The background was an ensemble average of 20 frames taken of an uncharged setup filled with SPQ-absent KCl solution. The flatfield was an ensemble average of the first 20 frames taken during an experiment before application of the electric field. We varied the magnitude of the step voltage applied at the start of an experiment, using voltages from 0.25 to 1.25 V. The latter range ensured observable desalination at all voltages yet prevented significant water electrolysis in the cell. Our source-meter power supply measured the current it supplied to the cell for the 1500 s after applying the step potential, with a sampling frequency of about 1 Hz.

RESULTS

Figure 2a and b, respectively, show plots of the measured salt concentration at equilibrium, c_{eq}, and measured equilibrium electric charge stored, q_{eq}, in the CDI cell versus V_{cell}. Measured equilibrium salt concentrations are obtained from SPQ fluorescence visualization data at 750 s after application of the cell voltage. At this time, SPQ fluorescence intensity (our signal of salt concentration) is largely constant in time (see Figure 3d). The charge stored is calculated by integrating the measured current versus time curve after subtracting the equilibrium leakage current (current at 1500 s; see Figure 4). We further normalized charge stored by the combined dry mass of the two electrodes (each electrode was about 10 mg) and present q_{eq} in units of C/g in Figure 2b. The model has three fitting parameters which are determined by comparing equilibrium concentration and charge data to the model predictions.[1,42] These parameters are the volumetric Stern layer capacitance, $C_{st,vol}$, (including its nonlinear dependence on charge, as described by the parameter α, see below), and the additional potential, μ_{att}, of our HCAM electrodes. We fit the measured equilibrium salt concentration and charge stored in our cell to equilibrium mD model results, and the results are shown, respectively, in Figure 2a and b. As shown in Figure 2, both equilibrium concentration and charge data are fairly well described by the equilibrium mD model results when using μ_{att} = 1.5 kT and $C_{st,vol,0}$ = 0.13 GF/m^3 and utilizing a charge-dependent Stern layer capacitance of the form $C_{st,vol} = C_{st,vol,0} + \alpha\sigma_{mi}^2$ with α = 30 F·m^3/mol^2. The latter values for $C_{st,vol,0}$, μ_{att}, and α are similar to those measured for activated carbon electrodes and carbide-derived carbons (CDC) electrodes.[1] For example, Zhao et al. determined that $C_{st,vol,0} \cong$ 0.12 GF/m^3, $\mu_{att} \cong$ 1.4 kT, and $\alpha \cong$ 17 F·m^3/mol^2 were the values which best described desalination data when using activated carbon electrodes over a wide range of feed salinities.[9,17]

On the basis of the data of Figure 2, the equilibrium salt adsorption measured at V_{cell} = 1.2 V and 50 mM initial concentration is about 0.12 mmol of KCl per gram of carbon or about 9 mg/g. The latter adsorption value is similar to reported values for previously used HCAM electrodes in NaCl solutions.[1,8]

In Figure 3, we present results of the spatially and temporally resolved measurements of salt concentration in the space between porous electrodes. We plot these results in spatiotemporal form, where the abcissa is the position in the cell, x (see Figure 1a), and the ordinate is time from application of the step voltage to the cell. The visualized domain spans the middle 1 mm of the 1.5 mm space between electrodes, and thus, x = 0.5 mm represents the cell midpoint. The colormap represents the measured salt concentration averaged along the y-direction (see Figure 1a). Orange represents the initial concentration, and lighter colors (e.g., yellow) represent lower salt content. Black iso-concentration lines are also shown on the plots, highlighting the desalination extent and dynamics. In Figure 3b, we show the measured early time desalination dynamics for the case of 50 mM KCl and V_{cell} = 0.75 V. In Figure 3d, we show the complete (to approximately steady state) measured dynamics for the case of 50 mM and V_{cell} = 1 V. As shown, iso-concentration lines typically have a concave shape, indicating that the lowest concentrations in the visualized separator space are typically closest to the electrode surface, and the highest concentration occurs near the center of the cell. For example, in Figure 3b, a concentration of 47.5 mM is achieved at the edges of the visualized region at ~70 s, but this concentration is only achieved in the center at ~120 s. As can be seen in Figure 3d, iso-concentration lines separated by 5 mM are more closely spaced at early times (indicating rapid concentration changes) and then become farther apart as the concentration approaches an equilibrium value.

In Figure 3a,c, we plot the transport model results in spatiotemporal form in order to compare the measured desalination dynamics (Figure 3b,d) with model results. The transport model (described by coupled eqs 7−9) was solved with commercially available finite element simulation software (Comsol Multiphysics 4.3, Burlington, USA). The model results show similar dynamics to the experimental results, providing evidence that our technique was effective in

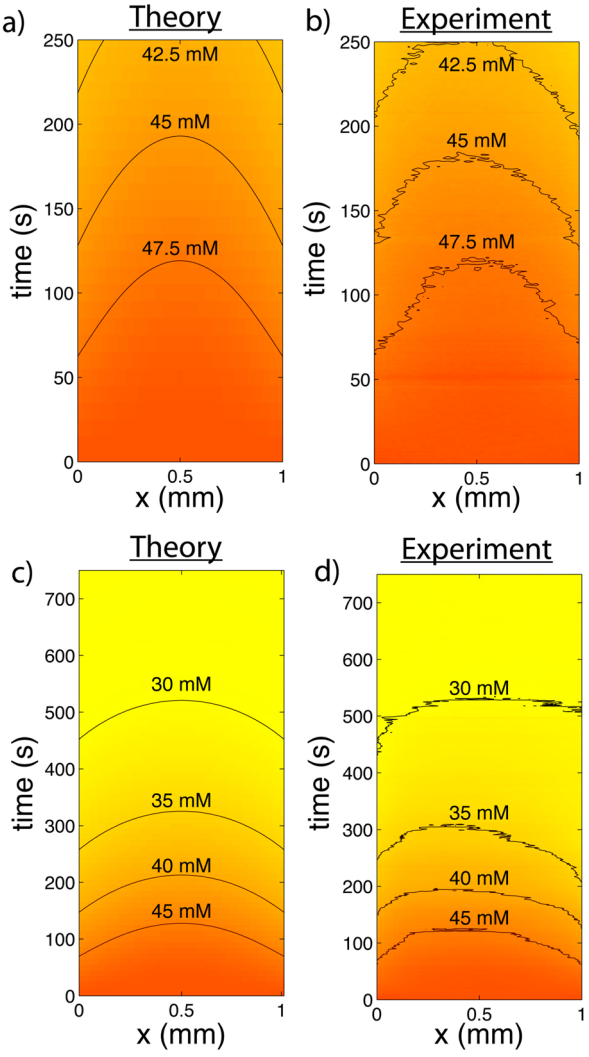

Figure 3. Spatiotemporal plots where, for predictions (parts a and c) and experiments (parts b and d), the colormap represents measured or predicted local salt concentration in the separator space. Salt concentration is plotted vs time, and the position between the two electrode, x (see Figure 1), and a step potential is applied at 0 s. Further, iso-concentration lines are shown as black curves. Part a shows the results from our porous electrode transport model for 50 mM salt and V_{cell} = 0.75 V, and b is the visualization data for 50 mM KCl and 0.75 V applied. Parts a and b show results up to 250 s and so focus on the early time dynamic response upon applying the cell voltage. Parts c and d are for the cases of 50 mM KCl and 1 V and show results up to 750 s, thus capturing the approach to equilibrium of the system.

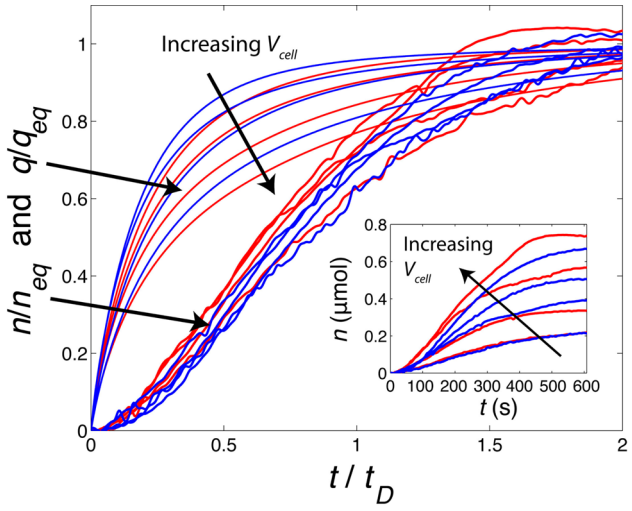

Figure 4. (a) Measurements of normalized salt removed from the visualized space between electrodes, n/n_{eq}, and normalized charge stored, q/q_{eq}, versus time nondimensionalized by the diffusion time across the separator half-width, t/t_D. Data includes results for initial concentrations of 80 mM (blue lines) and 50 mM KCl (red lines) and voltages of 0.5, 0.75, 1, and 1.25 V. Voltage is applied at t = 0 s. Normalizing n by n_{eq} causes an approximate collapse of these curves (see the dimensional data in the inset). Further, distinct differences are observed between the nondimensional cell charging (q/q_{eq}) and desalination (n/n_{eq}) dynamics. The cell charges quickly upon application of the electric field, reaching roughly 50% charged at a time of 0.25. Desalination requires longer times, as the space between electrodes is roughly only 10% desalted at a time of 0.25. Significant desalination occurs at times of approximately unity (the diffusion time), as $n/n_{eq} \cong 0.6$ at $t/t_D \cong 1$.

measuring salt dynamics in our CDI cell. Namely, the shape and location in time of the iso-concentration lines are fairly consistent between model and experiment. However, slight discrepancies between the predicted vs measured iso-concentration curves are observed between, for example, Figure 3c,d at times longer than 250 s. There are many potential sources for these discrepancies. One possible explanation for the asymmetry observed in the experimental data (but not the model results) is the effect of a native surface charge (zeta potential) of the HCAM electrodes. Whereas our model assumed zero native surface charge, the zeta potential of carbon-based materials in aqueous solutions is typically nonzero and can vary widely depending on pH of the solution and carbon material used.[43] A native zeta potential may lead to asymmetry in both charge efficiency and salt concentration profiles.[26] A second plausible explanation meriting further study is the potential for specific (nonelectrostatic) adsorption or desorption of the probe molecule during the experiment. As described in the Experimental Methods section, we allowed the HCAM electrodes to soak for 12 h in the KCl and probe solution before running experiments in an effort to reach equilibrium between the carbon surface and the solutes. However, there exists the possibility that the applied electric field may disturb the equilibrium between probe and carbon surface, causing additional specific adsorption/desorption which may affect results at long time scales. Further comparisons of experimental results to model results are shown in the Supporting Information document.

In Figure 4, we present solely experimental results of both total charge stored, q, in the CDI cell and total amount of salt removed from the visualized space, n, versus time nondimensionalized by the diffusion time across the separator half-width, $t_D = l_s^2/4D$ (the time-averaged salt adsorption kinetics of the HCAM electrodes were described in a previous publication[8]). Here, we show results for eight different experimental conditions, including initial KCl concentrations of 80 mM (blue lines) and 50 mM (red lines), and V_{cell} of 0.5, 0.75, 1, and 1.25 V. We further nondimensionalize n and q by their values at equilibrium (see Figure 2). The q/q_{eq} curves all rise up quickly upon application of the electric field, to reach a value of roughly 0.4 to 0.6 at t/t_D = 0.25. However, the n/n_{eq} curves react more sluggishly upon application of the cell voltage and only reach a value of about 0.1 at t/t_D = 0.25. This latter

dx.doi.org/10.1021/es403682n | Environ. Sci. Technol. 2014, 48, 2008−2015

observation suggests that, at these experimental conditions, desalination of the space between CDI electrodes upon application of a step voltage can be described roughly by a two-stage process: (1) the cell quickly (relative to t_D) charges and (2) at a later time, the space between electrodes begins to desalinate significantly. Further, in Figure 4, we observe that normalization of the time axis by the diffusion time approximately collapses the n/n_{eq} curves (see unscaled data in the inset). This suggests that the desalination dynamics in the space between electrodes is largely independent of applied voltage or concentration, an indication that the limiting transport mechanism governing this desalination is Fickian diffusion. A diffusion-limited desalination of the space between electrodes is also predicted from eq 7, as in the separator space, $p_{mi} = 0$ (noting eq 7 is only valid when the cation and anion diffusion coefficients are equal). We also note that the completion of the desalination process within this visualized space occurs at about the proposed diffusion time scale, t_D, as it is largely complete by about $2 \cdot t_D$.

There are at least two potential contributors toward explaining our observations of a delayed desalination of the space between electrodes (relative to cell charging). First, the ratio of salt uptake by EDLs in porous electrodes to the electric charge stored (i.e., the cell's charge efficiency) approaches zero at early times in the desalination process.[1,42] This latter phenomena is due to the finite current carried by EDL co-ions during the desalination process. In the mD model, charge efficiency grows with the hyperbolic tangent of the Donnan potential and so is smallest at early times in cell charging. As a result, despite significant EDL charging, potentially little desalination may occur soon after applying the step potential. Second, as suggested by our previous work,[8] the transport mechanism governing salt ion removal from the space between charging porous electrodes is Fickian diffusion into ion depleted electrode pores. This can lead to slow (relative to cell charging), diffusion-limited, desalination of the separator space.[8]

In conclusion, we have demonstrated for the first time an in situ measurement of spatially and temporally resolved chloride salt concentration between charging porous electrodes of a laboratory capacitive deionization (CDI) cell. Our measurements of salt concentration are in good agreement with the trends predicted by a multiscale porous electrode transport model using a modified Donnan formulation for EDL structure. Further, using these measurements, we observed that, at our experimental conditions, the desalination of the space between electrodes is significantly slower than cell charging. Direct visualization of salt concentration and gradients in CDI cells may in the future be used in studies including salts with unequal cation and anion mobilities (e.g., NaCl), unequal charge (e.g., Na_2SO_4), and the effects of electrolyte flow along or straight through the electrodes. We note that the measurement technique described here may not be appropriate for industrial systems generating potable water, as our technique involves adding low concentration SPQ probe to the salt solution of interest, which may affect water quality.

■ ASSOCIATED CONTENT

Supporting Information

Supporting information including additional model to data comparisons. This information is available free of charge via the Internet at http://pubs.acs.org/.

■ AUTHOR INFORMATION

Notes

The authors declare no competing financial interest.

■ ACKNOWLEDGMENTS

This work was supported by the National Science Foundation under Grant No. 0967600 and State of California's Proposition 50 funds administered by the Department of Water Resources. Any opinions, findings, and conclusions or recommendations expressed in this material are those of the authors and do not necessarily reflect the views of the National Science Foundation. M.E.S. would like to thank the Lawrence Scholar program and the Natural Sciences and Engineering Research Council (NSERC) of Canada for a postgraduate scholarship. Work at LLNL was performed under the auspices of the US DOE by LLNL under Contract DE-AC52-07NA27344.

■ REFERENCES

(1) Porada, S.; Zhao, R.; Van Der Wal, A.; Presser, V.; Biesheuvel, P. M. Review on the science and technology of water desalination by capacitive deionization. *Prog. Mater. Sci.* **2013**, *58*, 1388−1442.

(2) Rica, R. A.; Ziano, R.; Salerno, D.; Mantegazza, F.; Brogioli, D. Thermodynamic relation between voltage-concentration dependence and salt adsorption in electrochemical cells. *Phys. Rev. Lett.* **2012**, *109*, 156103.

(3) Wang, H.; Thiele, A.; Pilon, L. Simulations of cyclic voltammetry for electric double layers in asymmetric electrolytes: A generalized modified Poisson-Nernst-Planck model. *J. Phys. Chem. C* **2013**, *117*, 18286−18297.

(4) Giera, B.; Henson, N.; Kober, E. M.; Squires, T. M.; Shell, M. S. Model-free test of local-density mean-field behavior in electric double layers. *Phys. Rev. E* **2013**, *88*, 011301.

(5) Kim, T.; Yoon, J. Relationship between capacitance of activated carbon composite electrodes measured at a low electrolyte concentration and their desalination performance in capacitive deionization. *J. Electroanal. Chem.* **2013**, *704*, 169−174.

(6) Jande, Y. A. C.; Kim, W. S. Desalination using capacitive deionization at constant current. *Desalination* **2013**, *329*, 29−34.

(7) Garcia-Quismondo, E.; Santos, C.; Lado, J.; Palma, J.; Anderson, M. A. Optimizing the energy efficiency of capacitive deionization reactors working under real-world conditions. *Environ. Sci. Technol.* **2013**, *47*, 11866−11872.

(8) Suss, M. E.; Baumann, T. F.; Bourcier, W. L.; Spadaccini, C. M.; Rose, K. A.; Santiago, J. G.; Stadermann, M. Capacitive desalination with flow-through electrodes. *Energy Environ. Sci.* **2012**, *5*, 9511−9519.

(9) Zhao, R.; Biesheuvel, P. M.; van der Wal, A. Energy consumption and constant current operation in membrane capacitive deionization. *Energy Environ. Sci.* **2012**, *5*, 9520−9527.

(10) Lee, J.-B.; Park, K.-K.; Eum, H.-M.; Lee, C.-W. Desalination of a thermal power plant wastewater by membrane capacitive deionization. *Desalination* **2006**, *196*, 125−134.

(11) Liang, P.; Yuan, L.; Yang, X.; Zhou, S.; Huang, X. Coupling ion-exchangers with inexpensive activated carbon fiber electrodes to enhance the performance of capacitive deionization cells for domestic wastewater desalination. *Water Res.* **2013**, *47*, 2523−2530.

(12) Jeon, S.-I.; Park, H.-R.; Yeo, J.-G.; Yang, S.; Cho, C. H.; Han, M. H.; Kim, D.-K. Desalination via a new membrane capacitive deionization process utilizing flow electrodes. *Energy Environ. Sci.* **2013**, *6*, 1471−1475.

(13) Dlugolecki, P.; van der Wal, A. Energy recovery in membrane capacitive deionization. *Environ. Sci. Technol.* **2013**, *47*, 4904−4910.

(14) Blair, J. W.; Murphy, G. W. Electrochemical demineralization of water with porous electrodes of large surface area. In *Saline Water Conversion*; ACS Publications: Washington, DC, 1960; Vol. *27*, pp 206−223.

(15) Demirer, O. N.; Naylor, R. M.; Rios Perez, C. A.; Wilkes, E.; Hidrovo, C. Energetic performance optimization of a capacitive

deionization system operating with transient cycles and brackish water. *Desalination* **2013**, *314*, 130−138.
(16) Porada, S.; Bryjak, M.; van der Wal, A.; Biesheuvel, P. M. Effect of electrode thickness variation on operation of capacitive deionization. *Electrochim. Acta* **2012**, *75*, 148−156.
(17) Zhao, R.; Satpradit, O.; Rijnaarts, H. H. M.; Biesheuvel, P. M.; van der Wal, A. Optimization of salt adsorption rate in membrane capacitive deionization. *Water Res.* **2013**, *47*, 1941−1952.
(18) Bouhadana, Y.; Avraham, E.; Soffer, A.; Aurbach, D. Several basic and practical aspects related to electrochemical deionization of water. *AIChE J.* **2010**, *56*, 779−789.
(19) Farmer, J. C.; Fix, D. V.; Mack, G. V.; Pekala, R. W.; Poco, J. F. Capacitive deionization of NaCl and $NaNO_3$ solutions with carbon aerogel electrodes. *J. Electrochem. Soc.* **1996**, *143*, 159−169.
(20) Gabelich, C. J.; Tran, T. D.; Suffet, I. H. Electrosorption of inorganic salts from aqueous solution using carbon aerogels. *Environ. Sci. Technol.* **2002**, *36*, 3010−3019.
(21) Tsouris, C.; Mayes, R.; Kiggans, J.; Sharma, K.; Yiacoumi, S.; DePaoli, D.; Dai, S. Mesoporous carbon for capacitive deionization of saline water. *Environ. Sci. Technol.* **2011**, *45*, 10243−10249.
(22) Kim, Y.-J.; Choi, J.-H. Enhanced desalination efficiency in capacitive deionization with an ion-selective membrane. *Sep. Purif. Technol.* **2010**, *71*, 70−75.
(23) Xu, P.; Drewes, J. E.; Heil, D.; Wang, G. Treatment of brackish produced water using carbon aerogel-based capacitive deionization technology. *Water Res.* **2008**, *42*, 2605−2617.
(24) Li, H.; Zou, L.; Pan, L.; Sun, Z. Novel graphene-like electrodes for capacitive deionization. *Environ. Sci. Technol.* **2010**, *44*, 8692−8697.
(25) Cohen, I.; Avraham, E.; Noked, M.; Soffer, A.; Aurbach, D. Enhanced charge efficiency in capacitive deionization achieved by surface-treated electrodes and by means of a third electrode. *J. Phys. Chem. C* **2011**, *115*, 19856−19863.
(26) Avraham, E.; Bouhadana, Y.; Soffer, A.; Aurbach, D. Limitation of charge efficiency in capacitive deionization. *J. Electrochem. Soc.* **2009**, *156*, P95−P99.
(27) Suss, M. E.; Baumann, T. F.; Worsley, M. A.; Rose, K. A.; Jaramillo, T. F.; Stadermann, M.; Santiago, J. G. Impedance-based study of capacitive porous carbon electrodes with hierarchical and bimodal porosity. *J. Power Sources* **2013**, *241*, 266−273.
(28) Zhao, R.; van Soestbergen, M.; Rijnaarts, H. H. M.; van der Wal, A.; Bazant, M. Z.; Biesheuvel, P. M. Time-dependent ion selectivity in capacitive charging of porous electrodes. *J. Colloid Interface Sci.* **2012**, *384*, 38−44.
(29) Shkolnikov, V.; Santiago, J. G. A method for non-invasive full-field imaging and quantification of chemical species. *Lab Chip* **2013**, *13*, 1632−1643.
(30) Demirer, O. N.; Hidrovo, C. H. Laser-induced fluorescense visualization of ion transport in a pseudo-porous capcitive deionization microstructure. *Microfluid. Nanofluid.* **2014**, *16*, 109−122.
(31) Roelofs, S. H.; Soestbergen, M. v.; Odijk, M.; Eijkel, J. C. T.; Berg, A. v. d. Effect of pH waves on capacitive charging in microfluidic flow channels. *Ionics*, **2014**.
(32) Sharma, K.; Bilheux, H.; Walker, L.; Voisin, S.; Mayes, R. T.; Kiggans, J.; Yiacoumi, S.; DePaoli, D. W.; Dai, S.; Tsouris, C. Neutron imaging of ion transport in mesoporous carbon materials. *Phys. Chem. Chem. Phys.* **2013**, *15*, 11740−11747.
(33) Biesheuvel, P. M.; Fu, Y.; Bazant, M. Z. Diffuse charge and Faradaic reactions in porous electrodes. *Phys. Rev. E* **2011**, *83*, 061507.
(34) Biesheuvel, P. M.; Fu, Y.; Bazant, M. Z. Electrochemistry and capacitive charging of porous electrodes in asymmetric multicomponent electrolytes. *Russ. J. Electrochem.* **2012**, *48*, 580−592.
(35) Chang, Y. C.; Myerson, A. S. The diffusivity of potassium chloride and sodium chloride in concentrated, saturated, and supersaturated aqueous solutions. *AIChE J.* **1985**, *31*, 890−894.
(36) Probstein, R. F. *Physicochemical Hydrodynamics*, Second ed.; John Wiley & Sons, Inc.: Hoboken, NJ, 2004.
(37) Newman, J.; Tiedemann, W. Porous-electrode theory with battery applications. *AIChE J.* **1975**, *21*, 25−41.
(38) Baumann, T. F.; Worsley, M. A.; Han, T. Y. J.; Satcher, J. H. High surface area carbon aerogel monoliths with hierarchical porosity. *J. Non-Cryst. Solids* **2008**, *354*, 3513−3515.
(39) Biener, J.; Stadermann, M.; Suss, M.; Worsley, M. A.; Biener, M. M.; Rose, K. A.; Baumann, T. F. Advanced carbon aerogels for energy applications. *Energy Environ. Sci.* **2011**, *4*, 656−667.
(40) Illsley, N. P.; Verkman, A. S. Membrane chloride transport measured using a chloride-sensitive fluorescent probe. *Biochemistry* **1987**, *26*, 1215−1219.
(41) Shkolnikov, V.; Bahga, S. S.; Santiago, J. G. Desalination and hydrogen, chlorine, and sodium hydroxide production via electrophoretic ion exchange and precipitation. *Phys. Chem. Chem. Phys.* **2012**, *14*, 11534−11545.
(42) Porada, S.; Borchardt, L.; Oschatz, M.; Bryjak, M.; Atchison, J.; Keesman, K. J.; Kaskel, S.; Biesheuvel, P. M.; Presser, V. Direct prediction of the desalination performance of porous carbon electrodes for capacitive deionization. *Energy Environ. Sci.* **2013**, *6*, 3700−3712.
(43) Kinoshita, K. *Carbon: electrochemical and physicochemical properties*; John Wiley Sons: New York, NY, 1988.